nature communications

Article

https://doi.org/10.1038/s41467-025-57475-5

Thermo-responsive jamming by particle shape change

Received: 17 July 2024

Accepted: 21 February 2025

Published online: 07 March 2025

Check for updates

Jiawei Han[1], Peng Wang[1], Yu Guo[1,2] ✉, Thomas Pähtz[3], Zhaosheng Yu[1], Chuan-Yu Wu[4] & Jennifer S. Curtis[5]

Granular materials transition between unjammed (deformable) and jammed (rigid) states when adjusting their packing density. Here, we report on experiments demonstrating that the same kind of phase transition can be alternatively achieved through temperature-controlled particle shape change. Using a confined system of randomly-packed rod-like particles made of shape memory alloy (SMA), we exploit that shape recovery of these bent rods with rising temperature at a constant packing density leads to a jammed state. The responsible physical processes are elucidated with numerical simulations based on the Discrete Element Method. As an exemplary application of the uncovered mechanism, we engineer a smart clamp that can actively grip or release an object through the thermo-induced jamming or unjamming of the granular material, and robustly so under cyclic temperature changes. In the jammed state, its load-bearing capability surpasses the total SMA weight by a tunable margin, up to over 800-fold. The clamping design paves the way towards a new kind of functional devices based on the thermo-responsive jamming of shape memory granular materials.

Granular materials, which are assemblies of many discrete particles, exhibit complex behaviors that mimic, and transition between, those of solids, liquids, and gases[1–4], due to inherent microstructural disorder, heterogeneity, self-organization, and intricate interparticle contacts[5–8]. Leveraging these unique properties, smart devices that are simple to construct, robust to operate, and adaptable to different situations have been developed[9–15]. For instance, particle robotics has been developed to enable locomotion and transportation through the self-assembly of randomly-dispersed particles[9,10], while a recently invented granular actuator exploits the rapid and substantial volumetric expansion of granular materials[11,12]. Furthermore, granular grippers have emerged[13–15] through utilizing granular jamming, which refers to the transition from a flowing or disordered state to a solid-like state[16–23]. They offer the advantages of picking up objects of arbitrary shapes without the need for complex control and force sensing systems[13]. Likewise, the jamming of elongated fibers[24–26] and flat layers[27–29] has found application as a stiffening mechanism for soft robotics. Granular jamming is typically achieved through increasing the packing density and with it the shear resistance of the granular assembly[13–29]. However, triggering the jamming transition in industrial applications usually requires manual manipulation of a vacuum pump and pneumatic devices[30–37], a process that is difficult to automatize as these are complex systems involving many interacting functional parts.

Shape memory alloys (SMAs) and shape memory polymers are classified as smart materials because of their capability to revert to a predetermined shape when heated[38,39]. Thus, they are extensively utilized in smart devices and soft robotics, including robotic multi-fingered grippers[39–48], due to their unique feature of temperature-dependent shape change. Here, we show that this feature can be exploited to control a jamming transition of an assembly of discrete SMA rod-like particles. Such assemblies feature bulk behaviors of

[1]Department of Engineering Mechanics, State Key Laboratory of Clean Energy Utilization, Zhejiang University, Hangzhou 310027, China. [2]Huanjiang Laboratory, Zhuji, Zhejiang Province 311800, China. [3]Institute of Port, Coastal and Offshore Engineering, Ocean College, Zhejiang University, Zhoushan 316021, China. [4]School of Chemistry and Chemical Engineering, University of Surrey, Guildford GU2 7XH, UK. [5]Department of Chemical Engineering, University of California Davis, Davis, CA 95616, USA. ✉e-mail: yguo@zju.edu.cn

https://doi.org/10.1038/s41467-025-57475-5

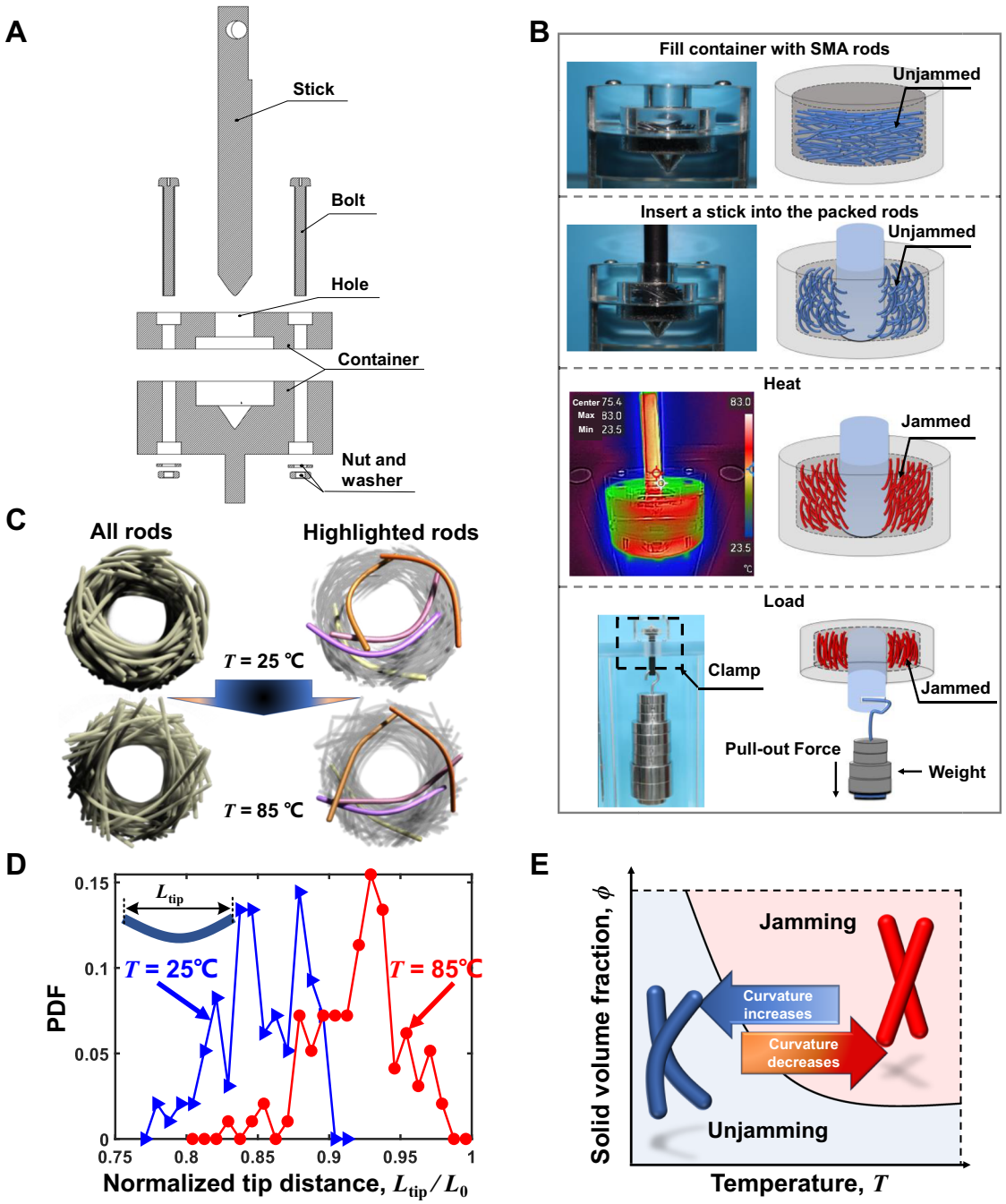

Fig. 1 | Operating principles of the clamp. A Schematic of the clamp components. **B** Clamping procedure. **C** XCT images of individual SMA rods of AR = 30 within the clamp container of solid volume fraction $\phi = 0.28$ at $T = 25\,°C$ and 85 °C. **D** Probability density function (PDF) of normalized tip distance L_{tip}/L_0 (where L_0 is the length of the SMA rod in its straight shape) for the SMA rods in the clamp container at $T = 25\,°C$ and 85 °C. **E** Illustration of unjamming-to-jamming phase transition based on the temperature T and solid volume fraction ϕ.

granular materials at the macroscopic scale, while simultaneously retaining the shape memory effect at the microscopic particle scale. This combination allows for unique functionalities and adaptability in potentially various applications.

To demonstrate this potential, we develop a simple and robust clamp (Fig. 1A and B). In contrast to previous jamming grippers, where the jamming transition was controlled by altering the particle packing density through a pneumatic system[13–15,24–29], the jamming or unjamming in our design is driven by temperature-induced changes in the SMA rod shapes. Consequently, the capacity of this clamp to hold or release weight is temperature-controlled. This property can be exploited by existing intelligent devices to respond to environmental changes merely with temperature adjustments, eliminating the necessity for human intervention. Notably, the clamp can hold a load exceeding 800 times the total weight of the SMA rods. This maximum clamping ability is tunable, depending on parameters such as solid volume fraction, rod aspect ratio (the ratio of rod length to diameter, AR), and the inclusion of small balls within the arrangement of packed rods. In addition to the experiments, a rod-like particle model considering the shape memory effect has been developed based on the Discrete Element Method (DEM), and numerical simulations are performed to give more particle-scale insights into this thermo-responsive jamming behavior.

Results

Design, fabrication, and operating principles

We create a tunable, temperature-controlled clamp utilizing SMA rod-like particles or rods. The operating principle is the thermo-responsive transition between the unjammed and jammed states, which is systematically investigated in this study through the analyses of the clamping performance and the mechanical behaviors of the SMA rods. The clamp consists of a cylindrical container (with an inner diameter of D_{in} = 32 mm and height of 15 mm) and a thin cylindrical stick (with a diameter of 14 mm and length of 120 mm), as illustrated in Fig. 1A. The operating procedure of the clamp is shown in Fig. 1B. A specified number of SMA rods (Supplementary Fig. 1A), fabricated from cut TiNi SMA wires, are randomly packed into the cylindrical container, which is closed using bolts and nuts. The SMA rods originally have a straight-line shape inside the container. The thin stick is then inserted through the hole into the container, causing the rods to bend. With the stick remaining inside, the rods are heated to an elevated temperature (e.g., 85 °C). Due to the shape memory effect, the heated rods tend to reduce their bending deformation. This decrease in the curvature of the rods leads to an unjamming-to-jamming transition of the granular system inside the container. Consequently, the inserted stick gets gripped by the jammed rods. A significant amount of weight can then be suspended from the stick using a hook. The load bearing capacity of the clamp at room temperature and a heated state is visualized in Supplementary Movie 1. In addition, a significant weight can be persistently held for more than 15 hours at a temperature of 80 °C (see Supplementary Movie 2), demonstrating good durability of the load bearing.

Using a 320 kV X-ray Computed Tomography (XCT) instrument, we obtain the three-dimensional (3D) images of the SMA rods within the clamp container, as depicted in Fig. 1C. The top row shows particle images at a low temperature of T = 25 °C, while the bottom row shows images at a high temperature of 85 °C. As the temperature increases, we observe changes in the overall structure of the packing, along with reductions in the bending deformations of the rods (or the rod curvatures), as shown by the highlighted rods. The SMA rods with AR = 25 ~ 40 and the present bending stiffness show no entanglement behaviors in the clamp container. To quantify rod bending deformation or curvature, we plot the probability density function (PDF) of the distance between two tips of a rod L_{tip} normalized by the length of the SMA rod in its straight shape L_0, in Fig. 1D. A larger L_{tip}/L_0 indicates smaller rod bending deformation and curvature. As illustrated, overall rod tip distances increase as the temperature rises from 25 °C to 85 °C.

The granular unjamming-to-jamming transition depends on solid volume fraction and temperature, which determines the rod curvature, as depicted in Fig. 1E. Jamming more likely occurs at larger solid volume fractions and smaller rod curvatures (at high temperatures). In the clamp container, the solid volume fraction remains constant during the clamping process, and a reduction in rod curvature due to rising temperature T leads to a transition to the jamming state. Conversely, when the temperature decreases from 85 °C to 25 °C, the rod bending deformation increases due to reduction in elastic modulus of the shape memory material, leading to an increase in rod curvature. Consequently, the granular system transitions to an unjammed state (Fig. 1E), resulting in the releasing of the weight. Thus, controlling the heating or cooling of SMA rods in the clamp container allows for the manipulation of weight holding or releasing mechanisms.

The effects of temperature and solid volume fraction

To assess the clamp performance, we experimentally measure the pull-out force on the thin stick using an INSTRON® universal testing machine (Supplementary Section S1 and Supplementary Fig. 2). The pull-out force is plotted in Fig. 2A as a function of stick displacement for various temperatures T at a solid volume fraction of ϕ = 0.28. The pull-out force rises rapidly to its peak and declines gradually with increasing stick displacement. Notably, the peak pull-out force increases with temperature. At T = 25 °C, the peak force is below 2 N, indicating an inability to bear a significant load. However, as the temperature T increases to 80 °C, the peak force exceeds 100 N. Furthermore, at a specified temperature of T = 80 °C, the peak pull-out force increases with increasing solid volume fraction ϕ, as illustrated in Fig. 2B. Using the temperature and solid volume fraction data, we construct a phase diagram in Fig. 2C, in which color represents the magnitude of the peak pull-out force F_{max}. In the previous studies of jamming of semiflexible polymers under homogeneous compressions, jamming was defined to occur when the pressure exceeds a threshold value[49]. Similarly, in the present study, a critical threshold force of $F_{max} = 10^4 m_{rod} g$, where m_{rod} is the mass of a rod and g is the gravitational acceleration, is used for the partition of unjamming and jamming states, and a boundary line with $F_{max} = 10^4 m_{rod} g$ (black dash line) is plotted in Fig. 2C. The critical volume fraction for jamming ϕ_c decreases and converges to a lower limit (ϕ_c = 0.1) with increasing temperature T. Thus, if the solid volume fraction ϕ is below 0.1, jamming never occurs regardless of temperature change. It should be noted that the pull-out force and critical volume fraction for jamming are dependent on the rod aspect ratio AR and container size, the effects of which will be discussed later.

Larger solid volume fractions ϕ cause stronger rod-rod and rod-boundary contacts, resulting in larger bending deformations, and thus smaller tip distances L_{tip}/L_0, of the rods (Fig. 2D). An angle α between the straight line connecting the two end tips of a bent SMA rod and the horizontal plane (x-z plane) represents the degree of the rod tilt[50], as illustrated in Fig. 2E. The inclination angle α can be calculated for each rod based on the XCT data. The mean inclination angles $\bar{\alpha}$ for the SMA rods of AR = 30 at various solid volume fractions ϕ are shown in Fig. 2F. It is observed that $\bar{\alpha}$ initially decreases and then increases with increasing ϕ at a specified temperature T = 80 °C, because more space exists for the rods to tilt more freely at a smaller solid volume fraction, and the larger contact forces at a larger solid volume fraction promote the rods to rotate and tilt more. For ϕ = 0.24, the mean inclination angle $\bar{\alpha}$ slightly increases when the temperature T increases from 25 °C to 80 °C, probably due to the increased contact forces propelling the tilt of the rods.

In order to probe the unjamming-to-jamming transition at the particle scale, we performed numerical simulations using the Discrete Element Method (DEM). A DEM model of SMA rod-like particles has been developed that considers the shape memory effect on the rod bending deformation. Detailed information on the DEM simulations and the model validation can be found in Supplementary Section S2. The computational set-up of the pull-out process of the stick from the assembly of SMA rods closely mimics the experimental set-up described above. Compared to the experimental studies, the DEM simulations are much less costly and time-consuming. In addition, contact forces between the rods and boundaries, which are difficult to measure in the experiments, can be easily obtained from the DEM simulations.

From the numerical simulations, various particle-scale information was obtained. The average normalized rod tip distance L_{tip}/L_0 gradually increases and converges to an upper limit with increasing temperature from 50 °C to 85 °C for each solid volume fraction ϕ (Fig. 2G). Additionally, this increase in L_{tip}/L_0 leads to a slight increase in the coordination number, defined as the average number of contacting neighbors per rod (Fig. 2H), and an increase in mean rod-rod and rod-boundary contact force $F_{con}/(E^M A)$ (Fig. 2G), in which E^M is the elastic modulus of the material at the martensite phase (the phase of SMA at low temperatures) and A is the rod cross-sectional area[51]. The larger coordination number and larger contact force both contribute to larger peak pull-out forces at higher T (Fig. 2A). As ϕ increases, both the coordination number and mean contact force increase (Fig. 2H and I), indicating stronger rod-rod contacts. Therefore, a denser packing with a larger ϕ leads to smaller L_{tip}/L_0 (Fig. 2D and G), corresponding to

https://doi.org/10.1038/s41467-025-57475-5

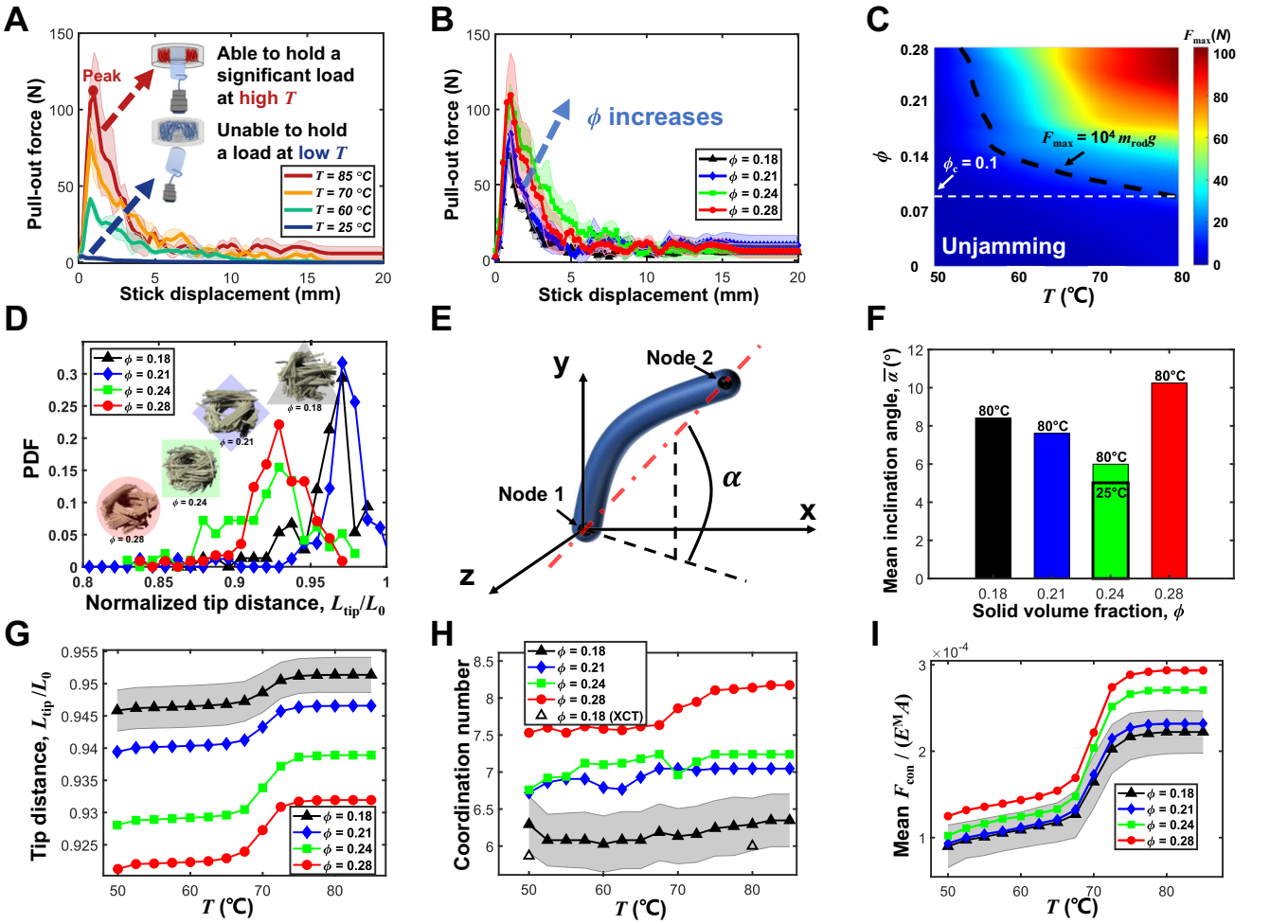

Fig. 2 | Effects of temperature T and solid volume fraction ϕ on clamp performance. A Pull-out force as a function of stick displacement for various temperatures at $\phi = 0.28$. **B** Pull-out force as a function of stick displacement for various solid volume fractions at $T = 80$ °C. **C** Phase diagram illustrating the peak pull-out force F_{max} based on T and ϕ. **D** Probability density function (PDF) of normalized tip distance L_{tip}/L_0 for the SMA rods at $T = 80$ °C and various solid volume fractions. **E** An illustration of inclination angle of a rod α. **F** Mean inclination angles of the SMA rods $\bar{\alpha}$ for various solid volume fractions at $T = 25$ °C and $T = 80$ °C. The results (**A**–**F**) are obtained from the experiments and XCT measurements. **G**, **H**, **I** Depict the results obtained from DEM simulations, showing the average normalized rod tip distance L_{tip}/L_0, coordination number, and mean contact force $F_{con}/(E^M A)$, respectively, as a function of temperature T for various ϕ values. The coordination numbers obtained from the XCT experiment are included in (**H**) for a comparison with the simulation results. The widths of shaded bands in the above figures represent the standard deviations from the mean values out of multiple measurements.

larger rod bending deformation, and larger peak pull-out forces (Fig. 2B).

At $\phi = 0.18$, five different packing configurations of the rods are generated in the simulations, and the pull-out test is simulated for each configuration. The mean rod tip distance, coordination number, and mean rod-rod contact force varying with the temperature T are shown in Fig. 2G, H, and I, respectively, in which the band widths of the shaded regions represent standard deviations from the mean values out of the five tests. In Fig. 2H, the experimental XCT results of the coordination numbers at $\phi = 0.18$ fall into the shaded region (standard deviations) of the simulation results, corroborating the DEM model.

To assess the robustness of the clamp performance, cyclic ascending-descending changes in temperature are applied to enable the clamp to repeatedly hold and release a weight. The testing procedure involves several steps.

Step 1: At room temperature of $T = 25$ °C, a thin cylindrical stick is inserted into the clamp container. At this point, it has no ability to lift a significant load (Fig. 2A).

Step 2: The temperature is increased to 80 °C to activate the clamping mechanism. A tensile test is performed using a universal testing machine to pull the thin stick out of the clamp container, and the pull-out force as a function of stick displacement is recorded.

Step 3: The clamp is cooled back to $T = 25$ °C and the thin stick is reinserted. At this low temperature, the clamp loses its ability to hold a significant load, just like Step 1.

Step 4: Steps 2 and 3 are repeated for multiple cycles to assess the clamp's robustness under cyclic temperature changes.

The pull-out force stick displacement curves at $T = 80$ °C exhibit qualitative similarity over different temperature-change cycles for a given solid volume fraction ($\phi = 0.24$, Fig. 3A). The peak pull-out forces vary between 85 and 115 N (Fig. 3B). The mean peak pull-out force at various ϕ is plotted in Fig. 3C, in which the band width of the shaded region represents one standard deviation from the mean for the results obtained from multiple heating-cooling cycles. It shows that the clamp demonstrates robust performance in bearing significant loads at high temperatures throughout cyclic temperature variation and repeated holding-releasing cycles.

The coordinates of the center of each rod can be experimentally determined by the XCT measurements. Thus, the displacement of the center of each rod relative to its initial position at the beginning of the temperature cycles δ can be obtained for a specified

https://doi.org/10.1038/s41467-025-57475-5

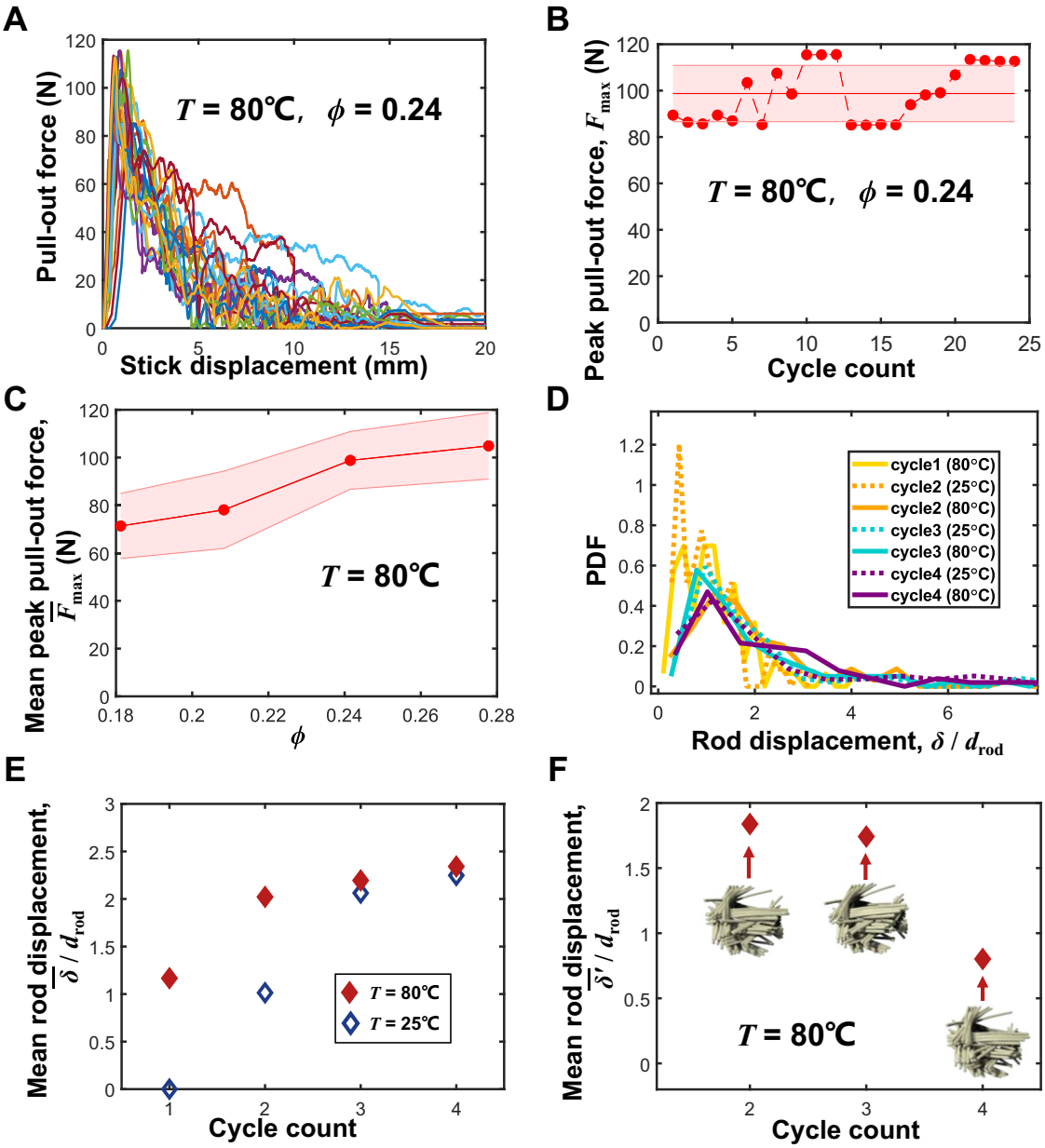

Fig. 3 | Clamping robustness subject to cyclic temperature changes. A Pull-out force as a function of stick displacement (colors are used to differentiate the results in different temperature cycles). **B** Peak pull-out forces F_{max} at $T =$ 80 °C and $\phi = 0.24$ across multiple temperature cycles. **C** Mean peak pull-out force $\bar{F}_{max}$ as a function of solid volume fraction ϕ. The widths of shaded bands in (**B**) and (**C**) represent the standard deviations from the mean values of the results at multiple temperature cycles. **D** Probability density function (PDF) of the SMA rod displacement relative to its initial position at the beginning of the temperature changes δ normalized by the rod diameter d_{rod} at $\phi =$ 0.18 over different cycles. **E** Mean rod displacement $\bar{\delta}/d_{rod}$ relative to its initial position as a function of temperature cycle count at $\phi =$ 0.18. **F** Mean rod displacement $\bar{\delta}'/d_{rod}$ relative to its position in the previous cycle as a function of temperature cycle count at $\phi = 0.18$ and $T =$ 80 °C.

temperature in each cycle. The probability density distribution of the rod displacement δ normalized by the rod diameter d_{rod} at $T = 25$°C and 80 °C in different cycles are plotted in Fig. 3D. It is observed that the tail curves of the large displacements of $\delta/d_{rod}>3$ nearly collapse at 80 °C, indicating the similar overall movement of the rods in different heating-cooling cycles. The average displacements of the rods $\bar{\delta}/d_{rod}$ (relative to the initial positions at the beginning of the temperature cycles) at $T = 25$ °C and 80 °C in different cycles can then be calculated as shown in Fig. 3E, and the average rod displacements $\bar{\delta}/d_{rod}$ increase and tend to converge to an upper limit of about 2.5 after multiple cycles. In addition, the average rod displacements relative to their positions at $T = 80$ °C in the previous cycle, $\bar{\delta}'/d_{rod}$, can be obtained in Fig. 3F, and it decreases below one after 4 cycles. For a specified temperature, as the rod displacements remain small in all the temperature cycles (Fig. 3E, F), the packing configuration and therefore peak pull-out forces exhibit slight changes across the cycles.

The effect of rod aspect ratio

SMA rods of various aspect ratios (ARs) are used in the clamp. The peak force as a function of AR at the temperature $T =$ 80 °C is shown in Fig. 4A. For a fixed ϕ, the peak pull-out force initially increases as AR increases from 25 to 30. Subsequently, it declines as AR continues to increase to 35 and 40. This nonmonotonic correlation likely reflects the AR-dependent microstructural properties of the rod packings in a confined space. Therefore, DEM simulations of the same processes as

https://doi.org/10.1038/s41467-025-57475-5

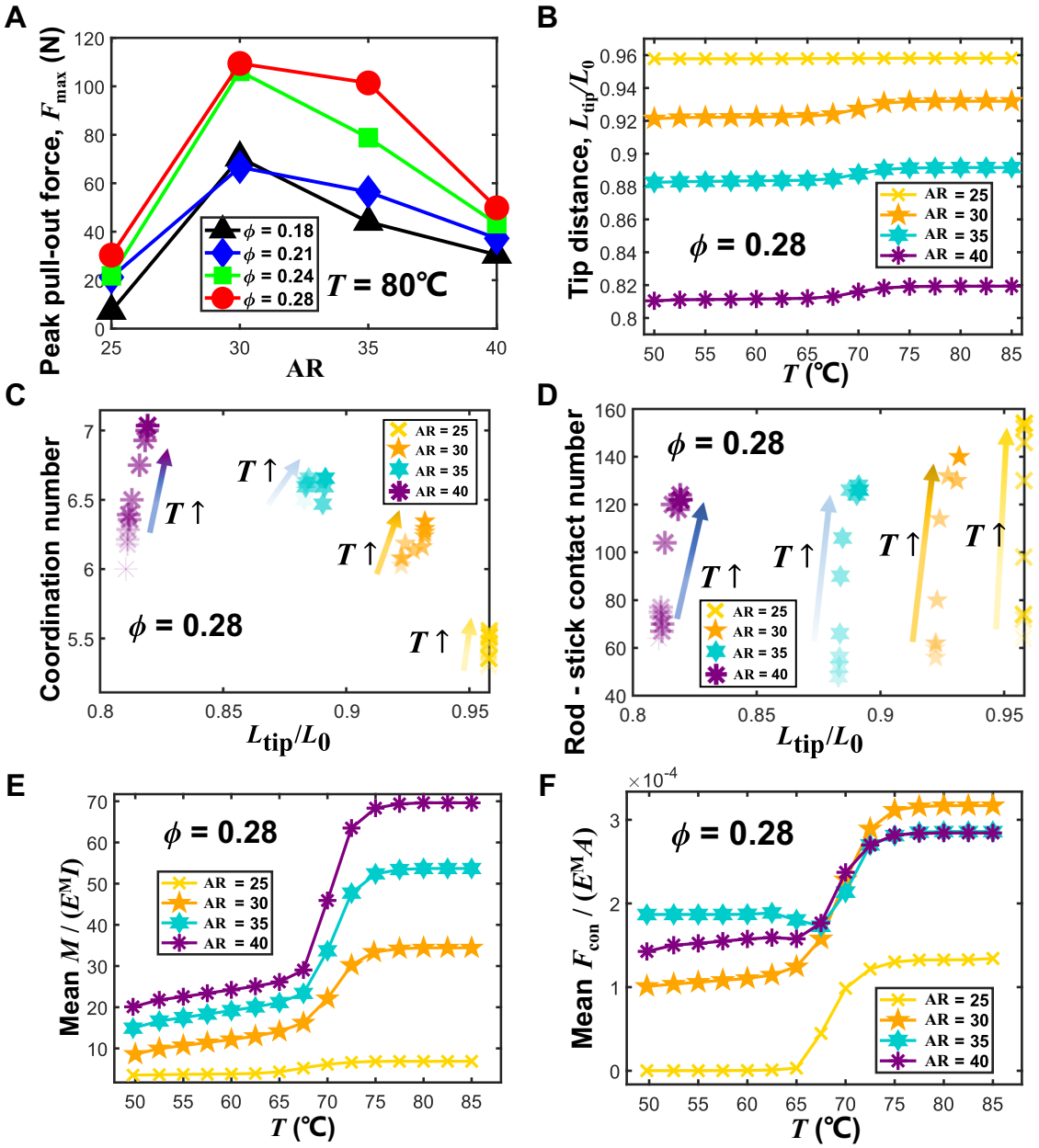

Fig. 4 | Effects of rod aspect ratio (AR) on clamp performance. A Experimental results of peak pull-out force F_{max} as a function of AR for various solid volume fractions ϕ. DEM simulation results of (**B**) average normalized rod tip distance L_{tip}/L_0 varying with temperature T, (**C**) coordination number and (**D**) SMA rod-stick contact number as a function of L_{tip}/L_0, (**E**) mean rod internal bending moment $M/(E^MI)$ and (**F**) mean contact force $F_{con}/(E^MA)$ varying with T.

the experiments are performed to unveil the microscopic information regarding the rod system within the clamp.

As T increases from 50 °C to 85 °C, the normalized rod tip distance L_{tip}/L_0 gradually rises (rods are recovering their original straight shape) and approaches an upper limit for each aspect ratio AR at $\phi =$ 0.28 as shown in Fig. 4B. Larger rod aspect ratio AR leads to smaller normalized tip distances L_{tip}/L_0 and thus larger rod bending deformation, as the larger AR rods need to bend more to accommodate themselves in the confined space of the clamp container. The dependences of coordination number and SMA-stick contact number on the normalized tip distance L_{tip}/L_0 are shown in Fig. 4C and D, respectively. Slight increases in L_{tip}/L_0 lead to substantial rises in coordination number and SMA-stick contact number, indicating that the rod shape change has a significant impact on the contact microstructures of the rod packings. In addition, at a specified T, the coordination number increases with increasing AR (Fig. 4C), which was also observed in the previous studies on the packing of flexible, elongated particles[52]. Due to the larger coordination number and boundary effect of the clamp container, the larger AR rods tilt more from the horizontal plane with larger inclination angles $\bar{\alpha}$ (Supplementary Fig. 14).

The normalized mean internal bending moment of the rods, $M/(E^MI)$, where I is area moment of inertia of the rod cross-sectional area, increases more significantly for larger aspect ratio rods as T increases (Fig. 4E). At a specified T, $M/(E^MI)$ increases monotonically with increasing AR, indicating that larger local bending deformations occur in larger AR rods due to the spatial constraint from the boundaries. The rod-rod and rod-boundary contact forces follow Weibull distributions (see Supplementary Section S3). The normalized mean contact force, $F_{con}/(E^MA)$, increases rapidly as the temperature T increases from 65 °C to 75 °C, during which the unjamming-to-jamming transition occurs for the rod system (Fig. 4F). In addition, the

https://doi.org/10.1038/s41467-025-57475-5

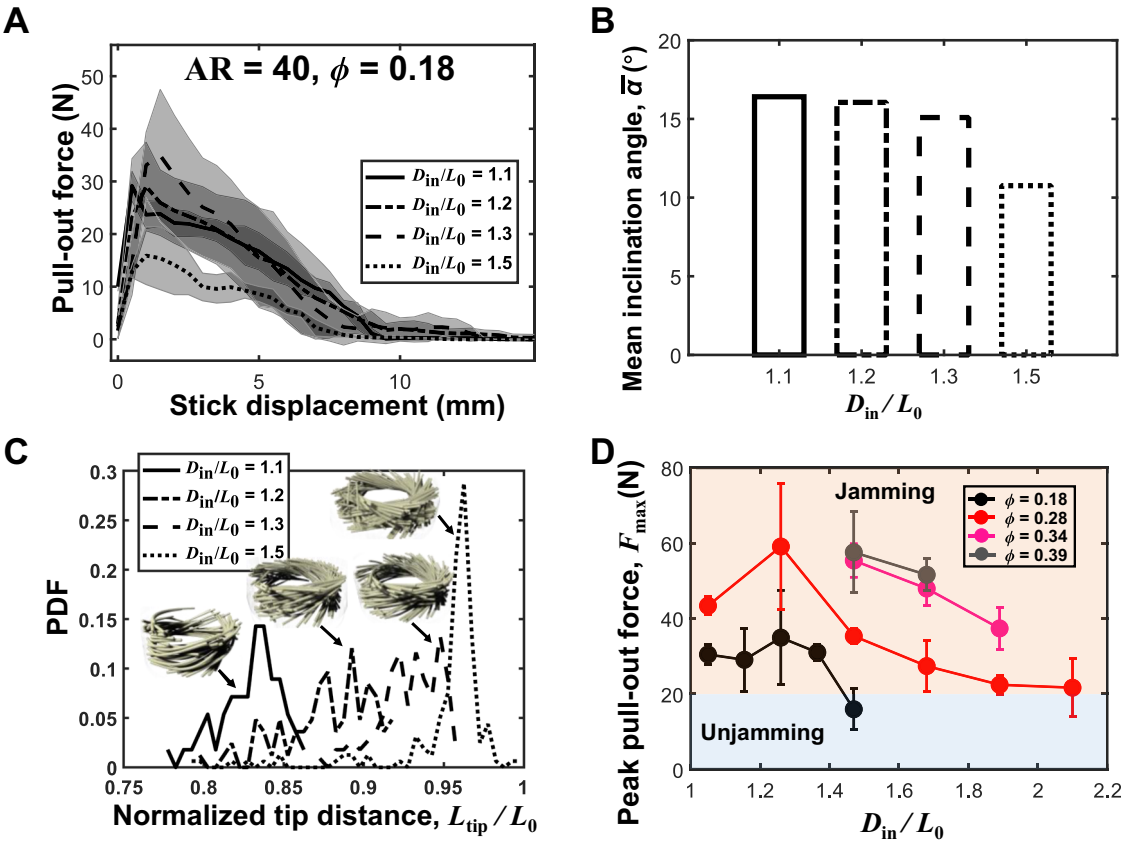

Fig. 5 | Effects of system size on clamp performance. A Pull-out force versus stick displacement for different normalized inner diameters of the clamp container D_{in}/L_0 at T=80 °C. **B** Variation of mean inclination angle $\bar{\alpha}$ with D_{in}/L_0 at T=25 °C. **C** Probability density function (PDF) of the normalized tip distance L_{tip}/L_0 for various D_{in}/L_0 at T=25 °C. **D** Peak pull-out force as a function of D_{in}/L_0 for various solid volume fractions ϕ at T=80 °C. The results are obtained from the experiments and XCT measurements of the rod systems with AR = 40. The band widths of shaded regions in **A** and lengths of error bars in **D** represent the standard deviations from the mean values out of multiple measurements.

mean contact force $F_{con}/(E^M A)$ exhibits a nonmonotonic dependence on AR.

At T = 80 °C, as AR increases from 25 to 30, although the SMA rod-stick contact number declines (Fig. 4D), a significant increase in the contact force occurs (Fig. 4F), leading to larger peak pull-out forces for AR = 30 (Fig. 4A). As AR increases from 30 to 35 and then 40 at T = 80 °C, both the SMA rod-stick contact number (Fig. 4D) and the mean contact force (Fig. 4F) decrease, resulting in a reduction in the peak pull-out force (Fig. 4A). Therefore, the effects of rod aspect ratio on clamp performance (Fig. 4A) originate from the microscopic properties (Fig. 4B–F) of the rod system.

The effect of system size

Different clamps with the various inner diameters of the container D_{in} are used in the experiments to explore the effect of system size. The rods of AR = 40 are arranged in the containers and the solid volume fraction is specified as ϕ = 0.18. The size ratio of the container diameter D_{in} to the real length of a rod L_0 has an impact on the pull-out forces (Fig. 5A): the peak pull-out force initially increases and then decreases with increasing size ratio D_{in}/L_0. The initial packing configuration and rod deformation are also affected by the container size. As D_{in}/L_0 increases, the constraint effects from the container boundaries are reduced. Consequently, the mean inclination of the rods $\bar{\alpha}$ declines (Fig. 5B) and normalized rod tip distance L_{tip}/L_0 increases (Fig. 5C) in the initial rod packings at T = 25 °C.

For various solid volume fractions ϕ, the peak pull-out force reaches a maximum at D_{in}/L_0 = 1.3 and it decreases with increasing D_{in}/L_0 for D_{in}/L_0 > 1.3 due to the reduced effects of the container boundaries. For the small containers with D_{in}/L_0 < 1.3, the number of the rods arranged in the container is so small that the number of the contacts between the SMA rods and the inserted stick is reduced as D_{in}/L_0 decreases, limiting the increase in the pull-out force exerted on the stick with the reduction of the container size. In the studies of the rod aspect ratio AR effects (Fig. 4), an increase in AR from 30 to 40, corresponding to a reduction in the size ratio D_{in}/L_0, leads to a decrease in the peak pull-out force, which is consistent with the results in Fig. 5. In addition, for a larger clamp container, a large peak pull-out force can be achieved by increasing the solid volume fraction ϕ (Fig. 5D).

Enhancing load-bearing capacity with the addition of small balls

The transition between unjamming and jamming states is the key mechanism underlying the ability of the clamp to either hold or release a weight. Therefore, it is natural to assume that adding small balls to fill the void spaces in a bed of elongated particles would stiffen the microstructure and enhance force transmission through the granular medium, thereby promoting the transition to the jamming state. To examine this hypothesis, experiments were conducted by introducing small glass balls with a diameter d_{ball} = 5 mm into the matrix of SMA rods within the clamp container (Fig. 6A). For a clamp with a constant volume fraction of SMA rods ϕ_{SMA} = 0.18, the addition of more small balls leads to an increase in the total solid volume fraction in the container $\phi_{ball+SMA}$. The pull-out force – stick displacement curves for various $\phi_{ball+SMA}$ values at T = 80 °C are shown in Fig. 6B. As observed from the insert, the peak pull-out force increases from 70 N to 100 N as the total solid volume fraction $\phi_{ball+SMA}$ increases from 0.18 to 0.45,

https://doi.org/10.1038/s41467-025-57475-5

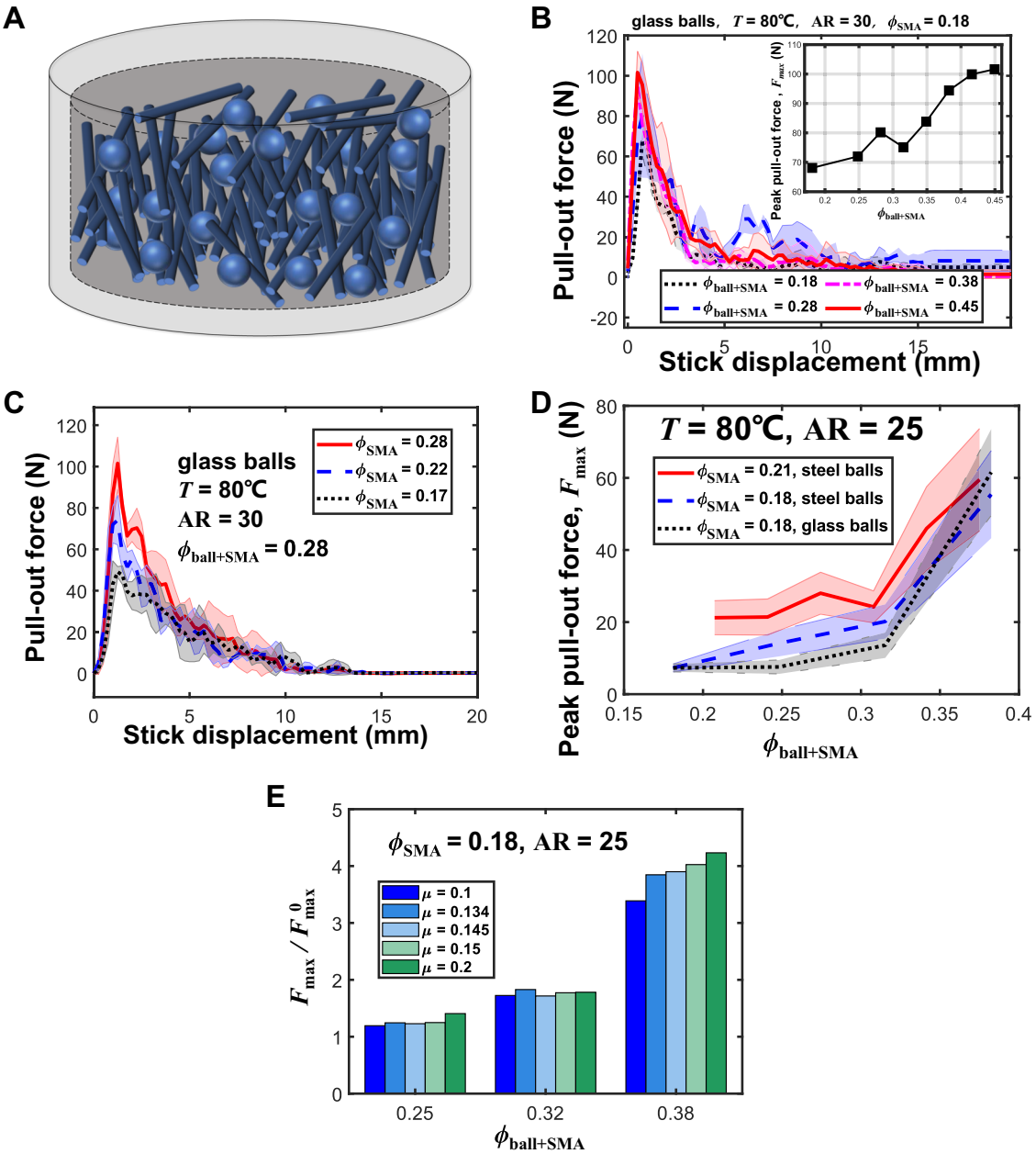

Fig. 6 | Clamping enhancement through addition of small balls to the packing of SMA rods. A An illustration with the addition of small balls. Experimental results of (**B**) pull-out force as a function of stick displacement for various overall solid volume fractions $\phi_{ball+SMA}$ and the variation of peak force with $\phi_{ball+SMA}$ for a specified volume fraction of SMA rods $\phi_{SMA} = 0.18$, (**C**) pull-out force as a function of stick displacement for various ϕ_{SMA} at a specified $\phi_{ball+SMA} = 0.28$, and (**D**) peak pull-out force F_{max} as a function of $\phi_{ball+SMA}$ with the addition of steel and glass balls. **E** Numerical simulation results of the normalized peak pull-out force F_{max}/F^0_{max} for various friction coefficients between SMA rods and steel balls, in which F^0_{max} is the peak pull-out force at $\phi_{SMA} = 0.18$ and $\phi_{ball} = 0$. The widths of shaded bands in (**B**–**D**) represent the standard deviations from the mean values out of multiple measurements.

demonstrating that the addition of small balls can, indeed, improve the load-bearing capability of the clamp by augmenting the clamp force at the jamming state.

With a constant total solid volume fraction of $\phi_{ball+SMA} = 0.28$, a larger fraction of SMA rods ϕ_{SMA} results in a larger peak pull-out force (Fig. 6C). Thus, the shape change of the SMA rods plays a more dominant role in the transition to jamming. When steel balls (Young's modulus $E_{ball} = 200$ GPa) are used to replace the glass balls ($E_{ball} = 72$ GPa) of the same diameter ($d_{ball} = 5$ mm), larger peak pull-out forces are obtained for the stiffer steel balls at intermediate overall solid volume fractions of $0.2 < \phi_{ball+SMA} < 0.35$ (Fig. 6D), and minor changes in the peak pull-out force occur with $\phi_{ball+SMA}$ smaller than 0.2 or greater than 0.35. In general, the small differences between with the steel and glass balls attribute to the much smaller Young's moduli of the SMA material ($E^A = 40$ GPa and $E^M = 20$ GPa), which determine the rod-ball contact stiffness.

In addition, it is observed that the peak pull-out force for a smaller fraction of SMA rods, $\phi_{SMA} = 0.18$, can catch up with that for $\phi_{SMA} = 0.21$ at a large overall solid volume fraction of $\phi_{ball+SMA} = 0.38$. In a very densely-packed granular bed, the shape changes of a few SMA rods can lead to strong rod-rod contacts due to significant space constraints. Therefore, fewer SMA rods are required to achieve satisfactory clamp performance for a densely-packed granular bed with a large overall solid volume fraction.

Furthermore, we also investigate the impact of friction between the balls and SMA rods. An inclined plane experiment is conducted to

measure friction coefficient between the spherical particles and SMA rods μ at different temperatures T (See Supplementary Fig. 4). At 80 °C, the mean friction coefficient between the glass balls and SMA rods ($\mu = 0.134$) is very close to that between the steel balls and SMA rods ($\mu = 0.145$). Thereafter, the DEM simulations are performed with μ varying between 0.1 and 0.2 (covering the range of friction coefficients experimentally measured). As shown in Fig. 6E, the scaled peak pull-out force, F_{max}/F^0_{max}, exhibits slight changes with μ at low solid volume fractions of $\phi_{ball+SMA} = 0.25$ and 0.32, while it increases significantly with μ at a larger $\phi_{ball+SMA} = 0.38$, in which a much stronger contact network is formed with more rod-ball contacts and larger contact forces (Supplementary Fig. 13).

Discussion

In summary, this article presents an innovative design of a tunable, temperature-controlled clamp based on the granular jamming of shape memory rods. The shapes of the rods within the clamp can change with temperature, facilitating a reversable unjamming-to-jamming transition. Consequently, the clamp can hold and release weight depending on the jamming and unjamming states, respectively. The load-bearing capacity of the clamp, which demonstrates robustness in holding and releasing performance under cyclic temperature variation, relies on the current temperature and the solid volume fraction of the rods within the clamp. Intermediate rod aspect ratios and intermediate size ratios of the clamp container diameter to the rod length yield the best clamp performance due to the combined effects of container boundaries and rod-stick contacts. Strengthening the contact force network is achieved by introducing small balls to fill the voids within the matrix of SMA rods, resulting in larger clamping forces. Thus, the peak clamp performance is maximized by increasing solid volume fraction, optimizing the rod aspect ratio and container size, and incorporating small balls to the packed rods.

Overall, the present clamp is developed based on a novel application of granular jamming induced by particle shape change, and the physical and engineering principles underlying this design can motivate innovations for smart devices using granular materials. In future, the roles that are played by particle ordering or organization, particle polydispersity, and temperature-dependent customized particle shapes (e.g. Z-shape, U-shape etc.) can be explored for a better understanding of the physics of such complex, thermo-responsive granular systems.

Methods

Materials

The clamp containers were made of polymethyl methacrylate (PMMA) and had an outer diameter of 80 mm and an outer height of 56 mm. The thin cylindrical sticks were fabricated from high-performance nylon (HP3DHR-PA12) using 3D printing technology and had a length of 120 mm. In the studies on the influences of temperature, solid volume fraction, and addition of small balls, the inner diameter of the container was 32 mm and the diameter of the thin stick was 14 mm. For the studies examining the effects of rod aspect ratio, the inner diameter of the container was 42 mm and the diameter of the thin stick was 32 mm, in order to accommodate the very large aspect ratio rods. For the studies of the effect of clamp container size, the inner diameters of the container were 42 mm, 46 mm, 50 mm, 55 mm, 59 mm, 67 mm, 76 mm, and 84 mm.

The shape memory rod-like particles were cut TiNi (nickel-titanium) alloy wires (Supplementary Fig. 1A) with a diameter of 1 mm and lengths of 25 mm, 30 mm, 35 mm, and 40 mm, respectively. For the TiNi alloy, the material density was 6500 kg m^{-3}, the elastic modulus at austenite (at high temperatures) phase (E^A) was 40 GPa, and the elastic modulus of the martensite phase (E^M) was 20 GPa. The austenitic start and finish temperatures (A^s and A^f) at zero stress were 50 °C and 80 °C (Supplementary Fig. 1B), respectively. The small balls used to fill the void space in the matrix of shape memory rods were made of steel (Young's modulus $E_{ball} = 200$ GPa) and glass ($E_{ball} = 72$ GPa), and they all had a diameter of 5 mm.

Temperature control

The DHG-9070A 250°C programmable blast drying oven (including a resistance heating tube, fan and air ducts, and a microcomputer intelligent controller, see Supplementary Fig. 3A) was used to heat the SMA rods for about 15 minutes from room temperature to the target temperature. During the pull-out tests using an INSTRON® universal testing machine, temperature-controlled silicone heating pads were used to maintain an almost constant temperature of the SMA rods in the container (Supplementary Fig. 3B). The temperature was monitored by a thermal imaging camera (Supplementary Fig. 3C). The maximum deviation from the target temperature should be less than 2 °C, otherwise the results would be discarded.

X-ray computed tomography

The clamp unit filled with SMA rod-like particles and a thin stick was scanned at a specified temperature using a 320 kV X-ray Computed Tomography (XCT) instrument. With the XCT data, 3D images of the individual SMA rods (Fig. 1C) were constructed using the image processing software Dragonfly®. In addition, utilizing the 3D data for each rod, the distance between the two tips of a rod L_{tip} and the inclination angle of a rod α were quantitatively determined to characterize rod curvature and orientation.

DEM simulations

For the Discrete Element Method (DEM) simulations, a new model was developed to simulate the behavior of the SMA rod-like particles, in which a temperature-dependent constitutive law was implemented to account for the shape memory effect on the rod bending deformation. To validate the simulations, cantilever bending of a single rod and a stick pull-out process from the granular clamp were analyzed. These simulations were performed using proprietary software developed at Zhejiang University, and more details regarding the DEM simulations are provided in Supplementary Section S2.

Data availability

The source data generated in this study are provided in the Source Data file. Source data are provided with this paper.

Code availability

The code for calculating temperature-dependent deformation of the shape memory rods based on the DEM method is deposited in GitHub under free access [https://github.com/HarryjwH/ShapeMemoryBond_DEM].

References

1. Guo, Y. & Curtis, J. S. Discrete element method simulations for complex granular flows. *Annu. Rev. Fluid Mech.* **47**, 21–46 (2015).
2. Jaeger, H. M., Shinbrot, T. & Umbanhowar, P. B. Does the granular matter? *Proc. Natl Acad. Sci.* **97**, 12959–12960 (2000).
3. Shen, Z. & Lintuvuori, J. S. Collective flows drive cavitation in spinner monolayers. *Phys. Rev. Lett.* **130**, 188202 (2023).
4. Vicsek, T. & Zafeiris, A. Collective motion. *Phys. Rep.* **517**, 71–140 (2012).
5. Junot, G., De Corato, M. & Tierno, P. Large scale zigzag pattern emerging from circulating active shakers. *Phys. Rev. Lett.* **131**, 068301 (2023).
6. Vicsek, T., Czirók, A., Ben-Jacob, E., Cohen, I. & Shochet, O. Novel type of phase transition in a system of self-driven particles. *Phys. Rev. Lett.* **75**, 1226 (1995).
7. Damasceno, P. F., Engel, M. & Glotzer, S. C. Predictive self-assembly of polyhedra into complex structures. *Science* **337**, 453–457 (2012).

8. Abdelrahman, M. K. et al. Material assembly from collective action of shape-changing polymers. *Nat. Mater.* **23**, 281–289 (2024).
9. Li, S. et al. Particle robotics based on statistical mechanics of loosely coupled components. *Nature* **567**, 361–365 (2019).
10. Li, S. et al. Programming active cohesive granular matter with mechanically induced phase changes. *Sci. Adv.* **7**, eabe8494 (2021).
11. Eristoff, S. et al. Soft actuators made of discrete grains. *Adv. Mater.* **34**, 2109617 (2022).
12. Liu, M., Fu, J. & Yang, S. Synthesis of microparticles with diverse thermally responsive shapes originated from the same janus liquid crystalline microdroplets. *Small* **19**, 2303106 (2023).
13. Brown, E. et al. Universal robotic gripper based on the jamming of granular material. *Proc. Natl Acad. Sci.* **107**, 18809–18814 (2010).
14. Amend, J. & Lipson, H. The JamHand: dexterous manipulation with minimal actuation. *Soft Robot.* **4**, 70–80 (2017).
15. Li, Y., Chen, Y., Yang, Y. & Wei, Y. Passive particle jamming and its stiffening of soft robotic grippers. *IEEE Trans. Robot.* **33**, 446–455 (2017).
16. Pillitteri, S., Lumay, G., Opsomer, E. & Vandewalle, N. From jamming to fast compaction dynamics in granular binary mixtures. *Sci. Rep.* **9**, 7281 (2019).
17. Liu, A. J. & Nagel, S. R. Jamming is not just cool any more. *Nature* **396**, 21–22 (1998).
18. Jin, Y., Urbani, P., Zamponi, F. & Yoshino, H. A stability-reversibility map unifies elasticity, plasticity, yielding, and jamming in hard sphere glasses. *Sci. Adv.* **4**, eaat6387 (2018).
19. Dashti, H., Saberi, A. A., Rahbari, S. H. E. & Kurths, J. Emergence of rigidity percolation in flowing granular systems. *Sci. Adv.* **9**, eadh5586 (2023).
20. Cates, M. E., Wittmer, J. P., Bouchaud, J. P. & Claudin, P. Jamming, force chains, and fragile matter. *Phys. Rev. Lett.* **81**, 1841 (1998).
21. Karuriya, A. N. & Barthelat, F. Granular crystals as strong and fully dense architectured materials. *Proc. Natl Acad. Sci.* **120**, e2215508120 (2023).
22. Behringer, R. P. & Chakraborty, B. The physics of jamming for granular materials: a review. *Rep. Prog. Phys.* **82**, 012601 (2018).
23. Liu, A. J. & Nagel, S. R. The jamming transition and the marginally jammed solid. *Annu. Rev. Condens. Matter Phys.* **1**, 347–369 (2010).
24. Brancadoro, M., Manti, M., Tognarelli, S. & Cianchetti, M. Fiber jamming transition as a stiffening mechanism for soft robotics. *Soft Robot.* **7**, 663–674 (2020).
25. Brancadoro, M., Manti, M., Tognarelli, S. & Cianchetti, M. Preliminary experimental study on variable stiffness structures based on fiber jamming for soft robots. in *2018 IEEE International Conference on Soft Robotics (RoboSoft)*. pp. 258-263 (IEEE, 2018).
26. Yang, B. et al. Reprogrammable soft actuation and shape-shifting via tensile jamming. *Sci. Adv.* **7**, eabh2073 (2021).
27. Ou, J. et al. jamSheets: Thin Interfaces with Tunable Stiffness Enabled by Layer Jamming. *Proceedings of the 8th International Conference on Tangible, Embedded and Embodied Interaction* 65-72 (2014).
28. Narang, Y. S., Vlassak, J. J. & Howe, R. D. Mechanically versatile soft machines through laminar jamming. *Adv. Funct. Mater.* **28**, 1707136 (2018).
29. Kim, Y.-J., Cheng, S., Kim, S. & Iagnemma, K. A novel layer jamming mechanism with tunable stiffness capability for minimally invasive surgery. *IEEE Trans. Robot.* **29**, 1031–1042 (2013).
30. Rus, D. & Tolley, M. T. Design, fabrication and control of soft robots. *Nature* **521**, 467–475 (2015).
31. Shah, D. et al. Shape changing robots: bioinspiration, simulation, and physical realization. *Adv. Mater.* **33**, 2002882 (2021).
32. Hines, L., Petersen, K., Lum, G. Z. & Sitti, M. Soft actuators for small-scale robotics. *Adv. Mater.* **29**, 1603483 (2017).
33. Shintake, J., Cacucciolo, V., Floreano, D. & Shea, H. Soft robotic grippers. *Adv. Mater.* **30**, 1707035 (2018).
34. Wang, Y., Li, L., Hofmann, D., Andrade, J. E. & Daraio, C. Structured fabrics with tunable mechanical properties. *Nature* **596**, 238–243 (2021).
35. Zhang, Z. et al. Soft and lightweight fabric enables powerful and high-range pneumatic actuation. *Sci. Adv.* **9**, eadg1203 (2023).
36. Zhang, Y., Zhang, W., Gao, P., Zhong, X. & Pu, W. Finger-palm synergistic soft gripper for dynamic capture via energy harvesting and dissipation. *Nat. Commun.* **13**, 7700 (2022).
37. Zhu, J. et al. Bioinspired multimodal multipose hybrid fingers for wide-range force, compliant, and stable grasping. *Soft Robot.* **10**, 30–39 (2023).
38. Tadaki, T., Otsuka, K. & Shimizu, K. Shape memory alloys. *Annu. Rev. Mater. Sci.* **18**, 25–45 (1988).
39. Roh, Y. et al. Vital signal sensing and manipulation of a microscale organ with a multifunctional soft gripper. *Sci. Robot.* **6**, eabi6774 (2021).
40. Wang, W. & Ahn, S.-H. Shape memory alloy-based soft gripper with variable stiffness for compliant and effective grasping. *Soft Robot.* **4**, 379–389 (2017).
41. Wang, W., Tang, Y. & Li, C. Controlling bending deformation of a shape memory alloy-based soft planar gripper to grip deformable objects. *Int. J. Mech. Sci.* **193**, 106181 (2021).
42. Linghu, C. et al. Universal SMP gripper with massive and selective capabilities for multiscaled, arbitrarily shaped objects. *Sci. Adv.* **6**, eaay5120 (2020).
43. Son, C., Jeong, S., Lee, S., Ferreira, P. M. & Kim, S. Tunable adhesion of shape memory polymer dry adhesive soft robotic gripper via stiffness control. *Robotics* **12**, 59 (2023).
44. Song, S., Drotlef, D.-M., Majidi, C. & Sitti, M. Controllable load sharing for soft adhesive interfaces on three-dimensional surfaces. *Proc. Natl Acad. Sci.* **114**, E4344–E4353 (2017).
45. Zhen, R., Jiang, L., Li, H. & Yang, B. Modular bioinspired hand with multijoint rigid-soft finger possessing proprioception. *Soft Robot.* **10**, 380–394 (2023).
46. Zhu, W. et al. A soft-rigid hybrid gripper with lateral compliance and dexterous in-hand manipulation. *IEEE/ASME Trans. Mechatron.* **28**, 104–115 (2022).
47. Chu, A. H., Cheng, T., Muralt, A. & Onal, C. D. A passively conforming soft robotic gripper with three-dimensional negative bending stiffness fingers. *Soft Robot.* **10**, 556–567 (2023).
48. Tang, Z., Lu, J., Wang, Z. & Ma, G. The development of a new variable stiffness soft gripper. *Int. J. Adv. Robot. Syst.* **16**, 1729881419879824 (2019).
49. Hoy, R. S. Jamming of semiflexible polymers. *Phys. Rev. Lett.* **118**, 068002 (2017).
50. Guo, Y., Wassgren, C., Hancock, B., Ketterhagen, W. & Curtis, J. Granular shear flows of flat disks and elongated rods without and with friction. *Phys. Fluids* **25**, 063304 (2013).
51. Guo, Y. et al. An investigation on triaxial compression of flexible fiber packings. *AIChE J.* **66**, e16946 (2020).
52. Rodney, D., Fivel, M. & Dendievel, R. Discrete modeling of the mechanics of entangled materials. *Phys. Rev. Lett.* **95**, 108004 (2005).

Acknowledgements

This work was financially supported by National Natural Science Foundation of China grant 12372250 (YG), National Natural Science Foundation of China grant 12132015 (YG), Zhejiang Provincial Natural Science Foundation of China grant LZ24A020002 (YG), and Specialized Research Projects of Huanjiang Laboratory grant XYY-128102-E52201 (YG). The pull-out experiments were conducted on the INSTRON® testing machine in Prof. Shaoxing Qu's Lab and technically supported by Dr. Qiyang Li in the Department of Engineering Mechanics at Zhejiang University. The X-ray computed tomography measurements were technically supported by Mr. Yu Peng in the Materials Microstructure Testing

Platform in the College of Civil Engineering and Architecture at Zhejiang University.

Author contributions

Y.G. conceptualized the study. J.H., P.W., Y.G., C.Y.W., and J.S.C. developed the methodology. J.H., Y.G., P.W., Z.Y., and T.P. conducted the investigation. J.H. and P.W. prepared the visualizations. Y.G., Z.Y., C.Y.W., and J.S.C. supervised the project. J.H. and P.W. drafted the original manuscript. Y.G., T.P., Z.Y., C.Y.W., and J.S.C. reviewed and edited the manuscript.

Competing interests

The authors declare no competing interests.

Additional information

Supplementary information The online version contains supplementary material available at https://doi.org/10.1038/s41467-025-57475-5.

Correspondence and requests for materials should be addressed to Yu Guo.

Peer review information *Nature Communications* thanks the anonymous reviewers for their contribution to the peer review of this work. A peer review file is available.